Synergistic cooperation between atomically dispersed Zn and Fe on porous nitrogen-doped carbon for boosting oxygen reduction reaction

Chuang Fu [a,b], Xueqiang Qi [a,c,*], Lei Zhao [b], Tingting Yang [a], Qian Xue [a], Zhaozhao Zhu [b], Pei Xiong [b], Jinxia Jiang [d], Xuguang An [e], Haiyuan Chen [b], Jun Song Chen [b,e], Andreu Cabot [c,f,**], Rui Wu [b,***]

[a] College of Chemistry and Chemical Engineering, Chongqing University of Technology, Chongqing 400054, China
[b] School of Materials and Energy, University of Electronic Science and Technology of China, Chengdu 611731, China
[c] Catalonia Institute for Energy Research (IREC), Sant Adrià de Besòs, Barcelona 08930, Spain
[d] Chongqing Medical and Pharmaceutical College, Chongqing 401331, China
[e] Institute for Advanced Study, Chengdu University, Chengdu 610106, China
[f] ICREA, Pg. Lluis Companys 23, 08010 Barcelona, Catalonia, Spain

A R T I C L E   I N F O

A B S T R A C T

A dual-atom catalyst (Zn/Fe-NC) is synthesized through pyrolyzing polyvinylpyrrolidone (PVP) coated on Fe-doped ZIF-8. Benefiting from a proper architecture and a synergistic effect between Zn and Fe sites, the Zn/Fe-NC catalyst provides an outstanding oxygen reduction reaction (ORR) activity, featuring a high half-wave ($E_{1/2}$) of 0.875 V versus reversible hydrogen electrode (RHE), excellent long-term stability with a negligible shift of $E_{1/2}$ (8 mV) after 10,000 cycles, and notable resistance to methanol in alkaline media. Density functional theory (DFT) calculation showed that the overpotential of ORR catalyzed by Zn/Fe-NC is only 0.282 V, and a slightly down-shifted d band center of active Fe affected by Zn significantly alleviates the adsorption of OH* intermediates, thus promoting the overall ORR electrocatalytic activity. Moreover, zinc-air batteries (ZABs) with Zn/Fe-NC catalyst as oxygen cathode display remarkable power density (186 mW cm^{-2}) and specific capacity (815 mAh g^{-1}), demonstrating great prospects for practical applications.

1. Introduction

Zinc-air batteries (ZABs) are attracting much interest related to their high energy density, potentially low cost, safe operation, and environmental friendliness [1–3]. However, their cathodic oxygen reduction reaction (ORR) suffers from inherently sluggish kinetics, resulting in high overpotentials and thus moderate round-trip efficiencies. Besides, the current most effective ORR catalysts are based on noble metals, whose high cost and poor stability severely hinder the practical application of ZABs [4–8]. Therefore, for this potentially cost-effective energy storage technology to reach the market, the development of inexpensive, active, and durable ORR catalysts is mandatory [9].

Recently, iron-nitrogen-carbon (Fe-N-C) single-atom catalysts (SACs) containing atomically dispersed Fe-N$_4$ active sites have shown considerable ORR catalytic performance associated with their highly unsaturated coordination bonds, maximized atomic utilization and strong quantum effects [10–16]. However, Fe-based SACs are limited by a moderate ORR activity associated with the too-strong binding of oxygen-containing intermediates [14]. A potential solution to this limitation is the introduction of a second metal-N$_4$ (M-N$_4$) active site that can modify the electronic structure or geometric configuration of the catalyst, thus improving ORR activity [11,17,18]. As an example, Ru-Co dual-atom catalysts display enhanced ORR ability due to synergistic modulation of the electronic structure and energy levels between the two transition metals [19,20]. A second illustrative example is that of N-coordinated Cu-Zn dual-atom catalysts that exhibit excellent activity and stability associated with a modulating effect of Zn on the orbital electron distribution of Cu. This electronic modulation facilitates the stretching and cleavage of O-O bonds on Cu active sites, thus accelerating the rate dominant step (RDS) of the ORR, the OOH* reduction

---

* Corresponding author at: College of Chemistry and Chemical Engineering, Chongqing University of Technology, Chongqing 400054, China.
** Corresponding author at: Catalonia Institute for Energy Research (IREC), Sant Adrià de Besòs, Barcelona 08930, Spain.
*** Corresponding author.
E-mail addresses: xqqi@cqut.edu.cn (X. Qi), acabot@irec.cat (A. Cabot), ruiwu0904@uestc.edu.cn (R. Wu).

[11]. Dual-atom catalyst can be obtained by direct pyrolysis of a mixture of metal salts with N and C precursors, followed by acid washing to remove metallic clusters/particles. However, beyond maximizing the number of catalytic sites and modulating their electronic levels, high-activity electrocatalysts require the active sites to be accessible at the triple-phase boundary, where the reactants and products can flow in and out. Thus, a proper catalyst architecture, offering a hierarchical pore structure must be rationally designed and engineered [21–25]. In this direction, metal-organic frameworks (MOFs) and particularly zeolite imidazole frameworks (ZIF) with rich carbon/nitrogen ligands, high specific surface areas, and built-in porous architectures, are ideal precursors to synthesize high-performance dual-atom catalysts [7,26–32].

Herein, we detail the synthesis of atomically dispersed Zn and Fe anchored on a 3D porous nitrogen-doped carbon (Zn/Fe-NC) by a self-sacrificing template and space-confinement strategy. We demonstrate the formation of Zn and Fe dual-atom active sites supported on a carbon frame with a honeycomb-like porous architecture and find that the obtained Zn/Fe-NC catalyst exhibits excellent ORR activity and stability. We further use the Zn/Fe-NC electrocatalyst as the air cathode in ZABs and demonstrate the assembled device to provide high peak power densities and specific capacities. The excellent results obtained are rationalized using density functional theory (DFT) calculations which show that the slightly down-shifted d band center alleviates the adsorption of OH* at the active Fe site, thus speeding up the potential-determination step (PDS) of OH* reduction reaction.

2. Experimental section

2.1. Chemicals

All chemical reagents including 2-methylimidazole (2-MeIm, 98 %), zinc nitrate hexahydrate ($Zn(NO_3)_2 \cdot 6\ H_2O$, 98 %), ferric chloride ($FeCl_3 \cdot 6\ H_2O$, 98 %), methanol (99.5 %), Nafion (5 wt%), polyvinylpyrrolidone (PVP, 1300000), potassium hydroxide (KOH, 85 %), and zinc acetate dihydrate (99 %, $Zn(CH_3COO)_2 \cdot 2\ H_2O$) were used directly without further purification.

2.2. Synthesis of Zn/Fe-NC

ZIF-8 particles were synthesized according to an impregnation method [33]. Typically, 1.487 g of $Zn(NO_3)_2 \cdot 6\ H_2O$ and 1.741 g of 2-MeIm were dissolved in 40 mL of methanol solution, respectively. The obtained solutions were mixed and incubated at 25 °C for 12 h. Subsequently, ZIF-8 particles were harvested after centrifugation and drying overnight.

For the synthesis of Zn/Fe-NC, 400 mg of ZIF-8 and 25 mg of $FeCl_3 \cdot 6\ H_2O$ were firstly dispersed in 30 mL of deionized water and stirred for 12 h at room temperature. Next, 50 mg of PVP was added and the solid-liquid mixture was stirred continuously for 6 h, followed by freeze-drying for two days to obtain Fe-doped ZIF-8 @PVP. Then, the collected samples were pyrolyzed under Ar atmosphere at 900 °C for 2 h. Finally, the Zn/Fe-NC catalyst was obtained after HCl (1 M) washing and drying. For comparison, Zn-NC and Zn/Fe-NC-50 were synthesized by a similar procedure without the addition of $FeCl_3 \cdot 6\ H_2O$ and with the addition of 50 mg of $FeCl_3 \cdot 6\ H_2O$, respectively.

2.3. Characterization

The morphologies of as-prepared samples were characterized by scanning electron microscopy (SEM, Phenom) and transmission electron microscopy (TEM, JEM2010F). X-ray diffraction (XRD,) patterns were obtained on a Bruker D8 Advance A25X using Cu Kg radiation to detect the crystal structure of as-prepared catalysts. The content of metals Zn and Fe was determined by inductively coupled plasma mass spectrometry (ICP-MS) on an Agilent 720ES. X-ray photoelectron spectroscopy (XPS) was conducted to analyze the chemical composition and valence

of the obtained catalysts on a Thermo Fisher Scientific system (Escalab 250Xi with AI Kα radiation). X-ray absorption spectroscopy (Fe K-edge/ Zn K-edge) was obtained in transmission mode at the Singapore Synchrotron Light Source center.

2.4. Electrochemical measurements

All electrochemical measurements were performed on an electrochemical workstation (Versa STAT 3, AMETEK) in three-electrode system, with a carbon rod (counter electrode), reference electrode (Hg/ HgO electrode), and a working electrode with diameters (5.0 mm). All potentials in this work were given relative to the reversible hydrogen electrode (RHE). The working electrode (catalyst loading of 0.5 mg cm^{-2}) was prepared as follows: 3 mg of catalyst in 600 μL isopropanol-aqueous mixed solution (isopropanol, deionized water and Nafion (5 wt %) in a volume ratio of 19:38:3) was sonicated for 60 min and 20 μL of fresh ink was dropped onto RDE electrodes. Pt/C catalyst loading capacity was designed to be 25 $μg_{Pt}\ cm^{-2}$. Cyclic voltammetry (CV) experiments were conducted from 0.05 to 1.2 V at 50 mV s^{-1} in N_2-saturated 0.1 M KOH solution. Linear scanning voltammetry (LSV) and rotating ring-disk electrode (RRDE) measurements were performed in O_2-saturated 0.1 M KOH solution with a sweeping rate of 10 mV s^{-1}. The stability of the catalyst was further investigated by an accelerated durability test (ADT), which was cycled 10,000 times at 0.6–1.0 V with 100 mV s^{-1} under O_2-saturated 0.1 M KOH electrolyte.

The electron transfer number (n) and kinetic parameters were calculated using the Koutecky-Levich equation as follows: [34,35].

$$\frac{1}{j} = \frac{1}{j_L} + \frac{1}{j_K} = \frac{1}{B\omega^{\frac{1}{2}}} + \frac{1}{j_K} \tag{1}$$

$$B = 0.62nFC_0(D_0)^{2/3}\nu^{-1/6} \tag{2}$$

$$j_K = nFKC_0 \tag{3}$$

where j, j_L and j_k are the measured current density, the diffusion-limiting and the kinetic current densities, respectively. ω is the electrode rotating rate, F is the Faraday constant (96,485 C mol^{-1}), C_0 presents the bulk concentration of O_2 in 0.1 M KOH solution (1.2 $\times 10^{-6}$ mol cm^{-3}), D_0 is the oxygen diffusion coefficient (1.9 $\times 10^{-5}$ $cm^2\ s^{-1}$) of 0.1 M KOH solution, and ν is the kinematic viscosity of 0.1 M KOH solution (0.01 cm^2 s^{-1}).

2.5. Zn-air battery tests

A homemade sandwich-like ZABs were assembled using a polished zinc plate as the anode, a carbon paper coated with Zn/Fe-NC as the air electrode, and a mixed electrolyte composed of 6 M KOH and 0.2 M Zn $(CH_3COO)_2 \cdot 2\ H_2O$. The catalyst ink was prepared by dispersing Zn/Fe-NC catalyst (2.5 mg) in ethanol (475 μL) and Nafion solution (5 wt%, 25 μL), followed by sonication for 30 min. Then 200 μL of the above catalyst ink was dropped onto carbon paper (1.0 cm^2) and dried naturally (catalyst loading: 1.0 mg cm^{-2}). The same catalyst loading was kept for Pt/C. The LSV polarization curves and galvanostatic discharge measurements were conducted on an electrochemical workstation (Biologic SP-150). The specific capacity of ZABs was calculated by the following equation:

$$\text{Specific Capacity} = \frac{\text{Current} * \text{service hours}}{\text{Weight of consumed zinc}} \tag{4}$$

2.6. Theoretical calculation

Spin-polarized DFT calculations were performed using Vienna Ab initio Simulation Package (VASP) [36]. The Perdew-Burke-Ernzerh (PBE) generalized gradient approximation (GGA) was used to describe the exchange-correlation functional. The projector-augmented wave

(PAW) method was used to deal with the ion-electron interactions. The plane wave energy cutoff was set as 400 eV and a $2 \times 2 \times 1$ Monkhorst-Pack k-point sampling was chosen. The convergence criteria of electronic energy and force were 1.0×10^{-5} eV and 0.02 eV/Å, respectively.

3. Results and discussion

3.1. Catalyst characterization

Fig. 1a shows a schematic of the synthetic procedure used to produce Zn/Fe-NC catalysts. Briefly, a Fe-doped ZIF-8 @PVP precursor was obtained by freeze-drying a mixture of ZIF-8, iron salt and PVP. In this step, ZIF-8 particles impregnated with Fe^{3+} ions were encapsulated into the PVP. Subsequently, the Fe-doped ZIF-8 @PVP precursor was annealed at 900 °C for 2 h under an Ar atmosphere. During this pyrolysis process, the ZIF-8 particles not only serve as self-sacrificial macro/mesopore templates to produce the porous carbon framework but also as the Zn source to form Zn sites upon their decomposition [37]. During this thermal process, a large part of the Zn evaporates, the Fe-impregnated ZIF-8 decomposes to yield a microporous carbon structure containing Zn and Fe, and the PVP matrix carbonizes to overall form a carbon-based hierarchical architecture [38–40]. In the last step, the material was washed with HCl to eliminate potential metal clusters or particles formed during the annealing process. As a reference, a Fe-free sample and a sample containing a double amount of Fe were produced using the same strategy and the two samples are referred to as Zn-NC and Zn/Fe-NC-50, respectively.
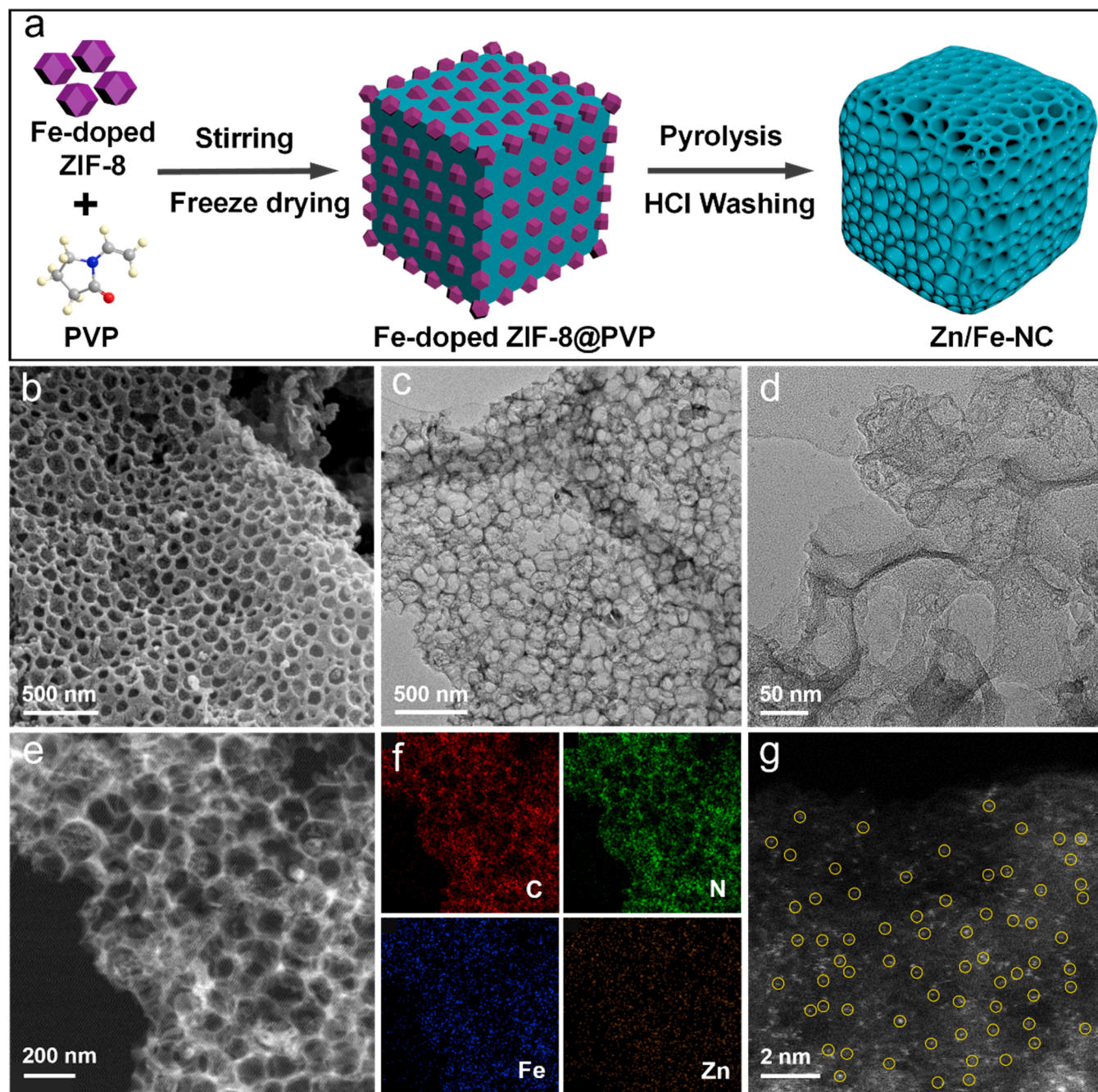

Fig. 1. (a) Schematic illustration of the synthesis for the Zn/Fe-NC catalyst. (b) SEM images of Zn/Fe-NC. (c, d) TEM image of Zn/Fe-NC. (e, f) HAADF-STEM image of Zn/Fe-NC and corresponding EDX elemental mappings. (g) AC-HAADF-STEM image of Zn/Fe-NC (yellow circles represented Zn and Fe single atoms).

As observed by SEM characterization (Fig. 1b), the obtained Zn/Fe-NC catalyst exhibited a honeycomb-like structure with an average pore size of 150 nm, consistent with the size of the initial ZIF-8 particles (Fig. S1). In contrast, as shown in Fig. S2a, Fig. S3a and Fig. S3b, the SEM and TEM images showed that the sample containing no Fe, Zn-NC maintained initial dodecahedral morphology of ZIF-8 instead of displaying a honeycomb structure after the annealing step. No any nanoparticles can be observed in the Zn-NC, and the EDX mapping analysis demonstrated that the C, N, O, and Zn elements were homogeneously distributed on the surface of Zn-NC (Fig. S3c and Fig. S3d). Besides, the sample containing a larger amount of Fe, Zn/Fe-NC-50 displayed the presence of larger and stacked blocks and numerous entangled carbon nanotubes (Fig. S2b-d). These results point to a key role of Fe in the carbon decomposition and pore-merging process. TEM images corroborated the hierarchical 3D architecture of Zn/Fe-NC (Fig. 1c). ICP-MS analysis showed the content of Fe and Zn on the Zn/Fe-NC to be 2.1 wt% and 0.65 wt%, respectively. However, extensive TEM, high-resolution TEM (HR-TEM), and High-angle annular dark field-scanning transmission electron microscopy (HAADF-STEM) characterization identified no metallic cluster or nanoparticle (Fig. 1d). On the other hand, HAADF-STEM analysis combined with energy dispersive x-ray (EDX) confirmed the presence of a homogeneous distribution of C, N, Zn and Fe elements on the carbon matrix (Fig. 1e and 1f). Besides aberration-corrected (AC) HAADF-STEM images displayed numerous isolated single-atom bright spots uniformly distributed throughout the carbon skeleton (Fig. 1g, Fig. S4a, and Fig. S4b) [41,42]. Thus, we conclude the Zn/Fe-NC contains a homogeneous distribution of atomically dispersed Zn and Fe.

The XRD patterns of Zn-NC and Zn/Fe-NC presented only two major diffraction peaks at approximately 26.3° and 43.6° (Fig. 2a), corresponding to the (002) and (101) planes of graphitic carbon, respectively. No XRD peak related to any Fe- or Zn-based crystal phase was observed for Zn-NC or Zn/Fe-NC catalysts, confirming the dispersion of Zn and Fe atoms throughout the nitrogen-doped carbon materials. However, when the content of Fe precursor was increased to 50 mg, i.e., for the Zn/Fe-NC-50 sample, a diffraction peak associated with metallic Fe (PDF# 06–0696) could be discerned at about 44.7° (Fig. S5), consistently with the XPS data shown latter. The presence of a Fe phase is related to an excess amount of Fe atoms that cannot be accommodated by the ZIF-8. Owing to the stronger Fe-Fe bond compared with Fe-N bonds, upon thermal annealing, large excesses of Fe aggregated to form Fe nanoparticles [43,44]. The Raman spectrum of Zn-NC, Zn/Fe-NC, and Zn/Fe-NC-50 displayed two distinct peaks at 1350 cm^{-1} and 1580 cm^{-1}, associated with disordered carbon (D band) and graphitic carbon (G band), respectively (Fig. 2b and Fig. S6) [45]. The I_D/I_G intensity ratios of Zn-NC, Zn/Fe-NC, and Zn/Fe-NC-50 were calculated to be 0.97, 0.94, and 0.96, respectively, indicating a slightly higher graphitization of the Zn/Fe-NC sample.

As shown in Fig. S7a and Fig. 2c, the Zn-NC displayed type I N_2 adsorption-desorption isotherm, indicating a micropore feature. In contrast, both Zn/Fe-NC and Zn/Fe-NC-50 showed a distinct type-IV isotherm with a characteristic hysteresis loop, indicating the presence of mesopores [46,47]. The Brunauer-Emmett-Teller (BET) specific surface area of Zn-NC, Zn/Fe-NC, and Zn/Fe-NC-50 was 904 m^2 g^{-1}, 571 m^2 g^{-1}, and 516 m^2 g^{-1}, respectively. The corresponding pore size distributions showed a mesoporous contribution at ca. 4 nm for both Zn/Fe-NC and Zn/Fe-NC-50 that we associate with a catalytic effect of Fe in the formation of the carbon porous structure (inset in Fig. 2c and Fig. S7b).

XPS analysis showed the C, N, O, Fe, and Zn atomic contents in Zn/Fe-NC were 85.3 %, 5.8 %, 8.6 %, 0.25 %, and 0.13 %, respectively (Fig. S8 and Table S1). The high-resolution C 1 s XPS spectrum was deconvoluted into three peaks, corresponding to C-C (~284.7 eV), C-N (~286.0 eV), and C-O (~288.9 eV), confirming the presence of heteroatoms N into the porous carbon matrix (Fig. S9a, Fig. S10, and Fig. S11a) [48]. The high-resolution N 1 s spectra of Zn-NC, Zn/Fe-NC, and Zn/Fe-NC-50 displayed the presence of four N species, including pyridine N (~398.6 eV), pyrrole N (~400.7 eV), graphite N (~401.5 eV), and oxidized N (~403.9 eV). Additionally, a peak at 399.8 eV was observed in both Zn/Fe-NC and Zn/Fe-NC-50, which was attributed to M-N_x (M=Fe and Zn) species (Fig. 2d, S9b and S11b) [49]. It is noted that Zn/Fe-NC possessed a higher proportion of pyridine N and graphite
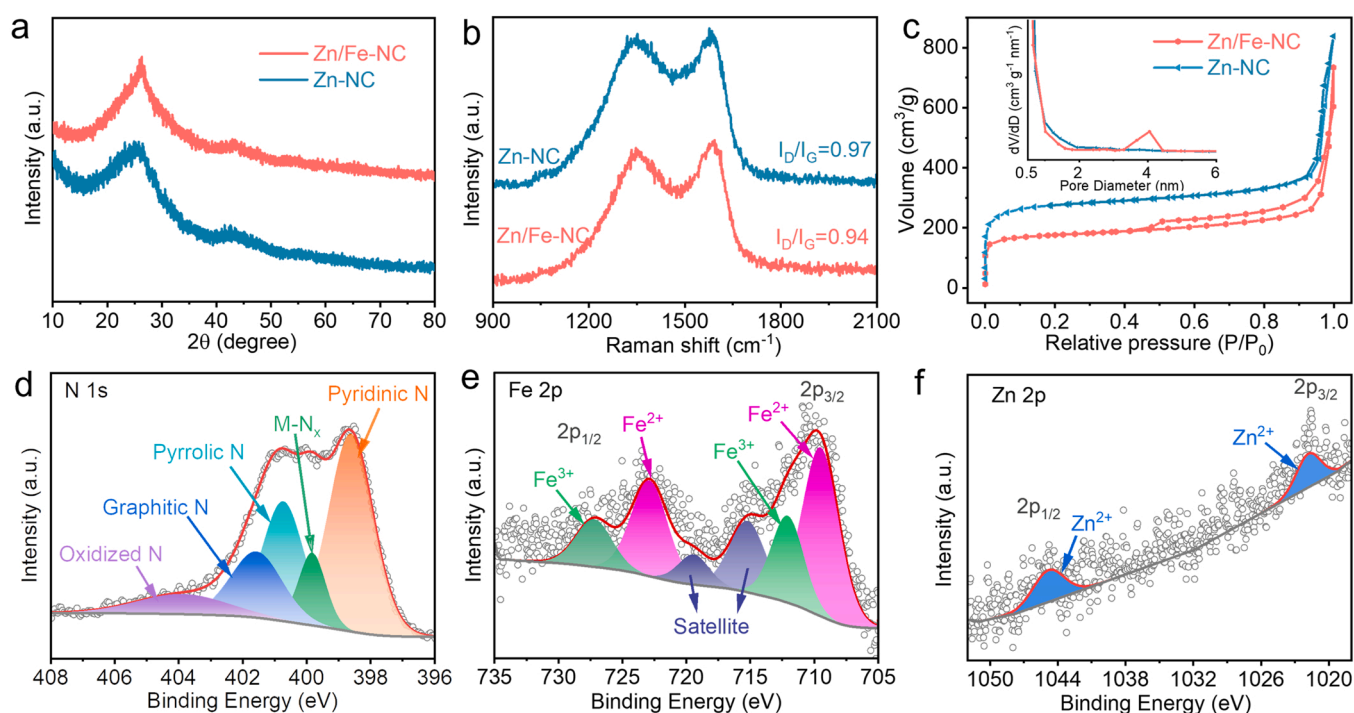

Fig. 2. (a) XRD patterns, (b) Raman spectra, and (c) N_2 adsorption-desorption isotherm of Zn-NC and Zn/Fe-NC. The inset shows the corresponding pore size distribution. (d-f) High-resolution XPS spectra of Zn/Fe-NC: (d) N 1 s, (e) Fe 2p, and (f) Zn 2p.

N compared to the Zn/Fe-NC-50 sample (Fig. S12). The high-resolution Fe 2p XPS spectrum (Fig. 2e and Fig. S11c) of Zn/Fe-NC was deconvoluted into a Fe^{2+} doublet at 709.5 eV ($2p_{3/2}$) and 722.8 eV ($2p_{1/2}$), a Fe^{3+} doublet at 712.1 eV ($2p_{3/2}$) and 727.2 eV ($2p_{1/2}$), and satellite peaks at 715.2 eV and 719.4 eV. No metallic Fe component was detected from the XPS spectrum of Zn/Fe-NC, but a Fe 2p doublet assigned to Fe^0 could be detected in the XPS Fe 2p spectrum of Zn/Fe-NC-50, consistently with XRD data [13,50,51]. The high-resolution Zn 2p spectrum (Fig. 2f, Fig. S9c, and Fig. S11d) of Zn/Fe-NC was fitted with just one doublet assigned to Zn^{2+} at 1021.8 eV ($2p_{3/2}$) and 1044.8 eV ($2p_{1/2}$) [11,52–54].

To further investigate the chemical state and coordination environment of Zn and Fe species in Zn/Fe-NC, X-ray absorption near-edge structure (XANES) and extended X-ray absorption fine structure (EXAFS) spectroscopic analysis were conducted [55]. As shown in Fig. 3a, the Zn K-edge XANES of Zn/Fe-NC was located between Zn foil and ZnO, suggesting that the Zn chemical valence state was between the two references. The Fourier transformed of extended X-ray absorption fine structure (FT-EXAFS) of Zn/Fe-NC exhibited a strong peak at 1.47 Å, which was assigned to the Zn-N(O) scattering path (Fig. 3b). Notably, no related peak of the Zn-Zn bond at 2.30 Å was observed in Zn/Fe-NC, further implying the absence of metallic Zn but the existence of atomically dispersed Zn [53,56]. The fitting EXAFS curves of Zn/Fe-NC in Fig. 3c uncovered that the coordination number of Zn

atoms was around 4 (Zn-N$_4$) (Table S2). In addition, the K-edge XANES of Fe in Zn/Fe-NC was located between those of FeO and Fe_2O_3 and close to that of FeO, suggesting that the valence state of Fe was near + 2 (Fig. 3d). The FT-EXAFS spectra showed that the major peak of Zn/Fe-NC at 1.50 Å corresponded to the Fe-N scattering path and there was no peak of Fe-Fe bond (2.2 Å), manifesting the atomically dispersed Fe throughout the whole Zn/Fe-NC sample (Fig. 3e) [13,57]. According to the EXAFS results (Fig. 3f), the coordination number between Fe and N in Zn/Fe-NC was around 4 (Fe-N$_4$) (Table S3). Moreover, the wavelet transform (WT) contour plots of both Zn and Fe showed the maximum intensity at around 4 Å^{-1} (Fig. 3g and Fig. S13a-e), corresponding to the respectively Zn-N and Fe-N coordination in Zn/Fe-NC [11,58,59].

3.2. Electrocatalytic performance

The ORR electrochemical performance of Zn/Fe-NC and the three reference materials, Zn-NC, Zn/Fe-NC-50, and a commercial Pt/C, was initially evaluated by CV and LSV in 0.1 M KOH solution. The CV curves of all these samples exhibited significant ORR peaks in O$_2$-saturated conditions, while no peaks were measured under N$_2$-saturated conditions (Fig. 4a and Fig. S14). Notably, the ORR peak of the Zn/Fe-NC was at 0.810 V, a significantly more positive potential than the reference samples including the commercial Pt/C catalyst, indicating a superior ORR activity. As shown in Fig. 4b and Fig. S15, among the tested
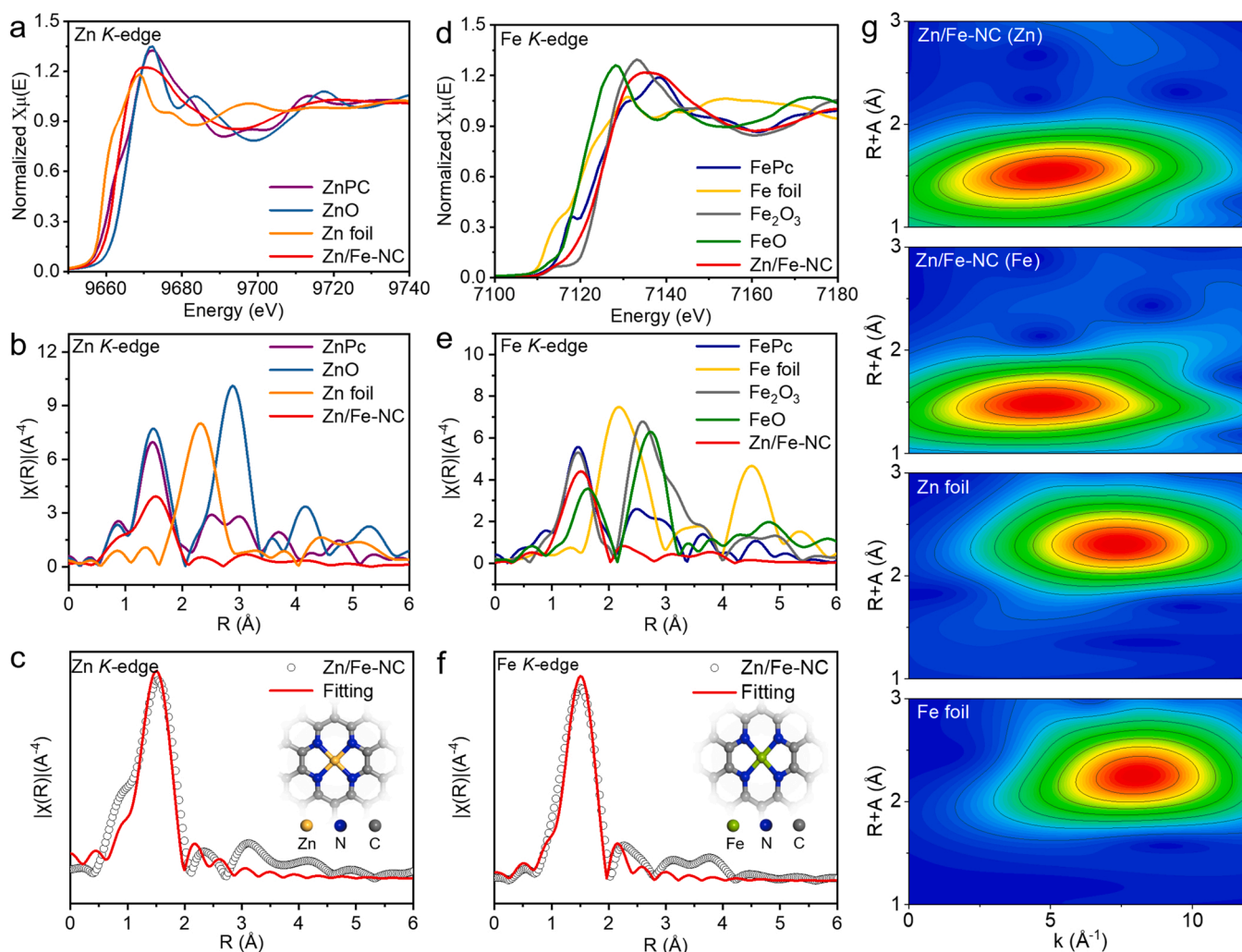

Fig. 3. (a) Zn K-edge XANES and (b) FT-EXAFS spectra of Zn/Fe-NC, Zn foil, ZnO and ZnPC. (c) FT-EXAFS fitting curves of Zn K-edge for Zn/Fe-NC. (d) Fe K-edge XANES and (e) FT-EXAFS spectra of Zn/Fe-NC, Fe foil, FeO, Fe$_2$O$_3$ and FePC. (f) FT-EXAFS fitting curves of Fe K-edge for Zn/Fe-NC. (g) WT contour plots for Fe foil, Zn foil, Zn/Fe-NC(Fe) and Zn/Fe-NC(Zn) at R space.
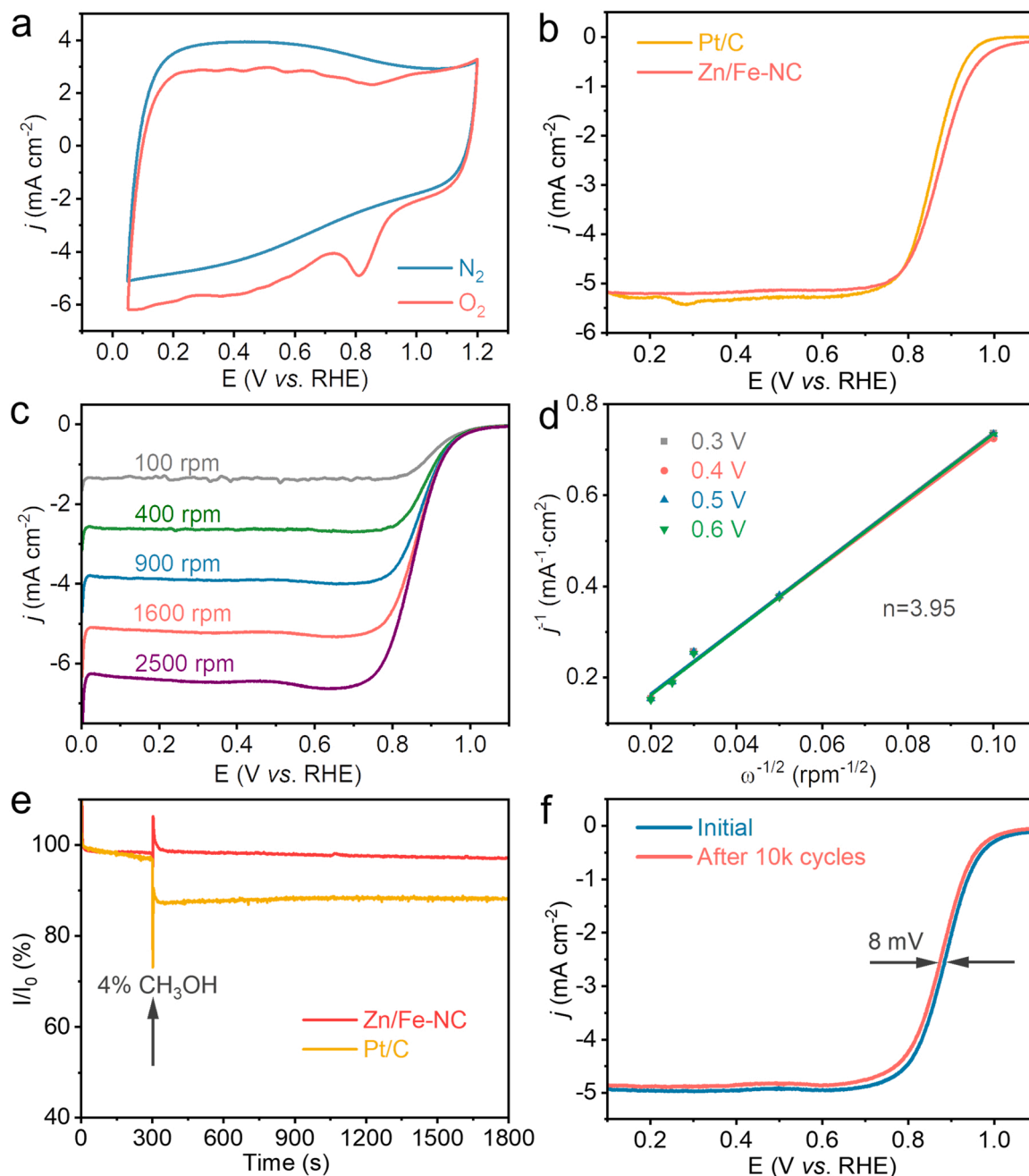
Fig. 4. (a) CV curves of Zn/Fe-NC in N_2- and O_2-saturated 0.1 M KOH solution. (b) LSV curves of Pt/C and Zn/Fe-NC in O_2-saturated 0.1 M KOH solution at 10 mV s^{-1} and 1600 rpm. (c) RDE curves at various rotating speeds for Zn/Fe-NC and (d) corresponding K-L plots at 0.3–0.6 V. (e) Chronoamperometric response for Zn/Fe-NC and Pt/C at 0.4 V upon addition of 4 vol% methanol in O_2-saturated 0.1 M KOH solution (1600 rpm) at 300 s (f) ORR polarization curves of Zn/Fe-NC before and after 10,000 cycles.

catalysts, Zn/Fe-NC displayed the best activity with an onset potential (E_{onset}) of 1.081 V, a half-wave potential ($E_{1/2}$) of 0.875 V and a diffusion limited current densities (j_L) of 5.202 mA cm^{-2}, which were much better than those of commercial Pt/C, pure Zn-NC and Fe-NC, even exceeding most state-of-the-art non-precious metal electrocatalysts (Table S4). This result proves that the synergistic cooperation between Zn and Fe atoms in Zn/Fe-NC catalyst has a positive effect on boosting ORR catalytic reaction.

On the other hand, a higher Fe content deteriorated the ORR performance, as observed for the Zn/Fe-NC-50 catalyst displaying an E_{onset} and $E_{1/2}$ of 0.994 V and 0.855 V, respectively. Besides, Zn/Fe-NC displayed a maximum kinetic current density of 10.1 mA cm^{-2} at 0.85 V, well above that of Pt/C (6.83 mA cm^{-2}), Zn-NC (0.967 mA cm^{-2}), and

Zn/Fe-NC-50 (5.38 mA cm^{-2}) (Fig. S16). Furthermore, The ECSA was obtained from the double-layer capacitance (C_{dl}) determined by CV from 20 to 100 mV s^{-1} (Fig. S17a-b) [60]. As shown in Fig. S17c, the C_{dl} of Zn/Fe-NC is 16.0 mF cm^{-2}, which is higher than that of Zn/Fe-NC-50 (13.2 mF cm^{-2}), suggesting more exposed active sites in Zn/Fe-NC [53].

To understand the ORR reaction process on the Zn/Fe-NC catalysts, RDE tests were carried out at different speeds, from 100 to 2500 rpm (Fig. 4c). As depicted in Fig. 4d, the Koutecky-Levich (K-L) plots of Zn/Fe-NC at various potentials exhibited good linearity and almost unchanged slope, indicating first-order kinetics. The calculated average electron transfer number of Zn/Fe-NC was about 3.95, revealing a close ideal four-electron ORR pathway, which was further confirmed by the RRDE tests (Fig. S18a). The H_2O_2 yield of Zn/Fe-NC was calculated to be

less than 5 % in the range of 0.2–0.8 V, corresponding to an average electron transfer number of 3.9–4.0 (Fig. S18b), confirming the efficient four-electron ORR pathway.

The methanol toxicity of Zn/Fe-NC and Pt/C catalysts was evaluated in an O_2-saturated 0.1 M KOH solution at a constant potential of 0.4 V. As shown in Fig. 4e, after adding 4 vol% of methanol, the cathode current of the Zn/Fe-NC catalyst showed a much slighter variation (2.76 %) than the commercial Pt/C catalyst (11.9 %), demonstrating a notable tolerance to methanol. Moreover, the long-term chronoamperometry tests for Zn/Fe-NC and commercial Pt/C were performed in 0.1 M KOH solution at a constant potential of 0.6 V. As shown in Fig S19, the Zn/Fe-NC catalyst decayed only 11.1 % of its initial current density after 40 h of continuous operation, while Pt/C attenuated 26.7 %, indicating that Zn/Fe-NC has much better durability. The ORR long-term stability of Zn/Fe-NC and Pt/C was further investigated by accelerated durability testing (ADT) between 0.6 and 1.0 V in an O_2-saturated 0.1 M KOH solution. After 10,000 cycles, the $E_{1/2}$ of the Zn/Fe-NC catalyst decayed only 8 mV, which was significantly better than that of Pt/C (39 mV), demonstrating superior durability in alkaline media (Fig. 4f and Fig. S20).

3.3. Theoretical computation

DFT calculations were performed to study the active sites and their synergistic effects. The four electron ORR pathways (i.e., $O_2 + * \rightarrow OOH^* \rightarrow O^* \rightarrow OH^* \rightarrow * + OH^-$) proceeded on Zn-$N_4$, Fe-$N_4$, and Zn-$N_4$/Fe-$N_4$ models were investigated under alkaline conditions (Fig. S21). The change of Gibbs free energy (ΔG) during the ORR process was calculated at U = 0 V and U = 1.23 V, respectively. As shown in Fig. 5a, all downhill reaction pathways revealed that all electron transfer steps on Zn-NC, Fe-NC, and Zn/Fe-NC can proceed spontaneously and exothermically at U = 0 V [61]. With U increasing to 1.23 V (Fig. 5b), the PDS for the Zn-NC catalyst was the reduction of OOH* and the overpotential was 1.08 eV. However, the PDS for both Fe-NC and Zn/Fe-NC was the reduction reaction of OH*, and the overpotential was significantly reduced to 0.438 eV and 0.282 eV, respectively. The PDS difference of Fe-NC and Zn/Fe-NC catalysts from that of Zn-NC, and the lowest overpotential of ORR catalyzed by dual-atom Zn/Fe-NC catalyst manifest that the existence of Zn atom promotes the catalytic activity of Fe atom in the Zn/Fe-NC catalyst. To further investigate the underlying origin of the synergistic effect of Zn/Fe-NC in ORR, the electronic
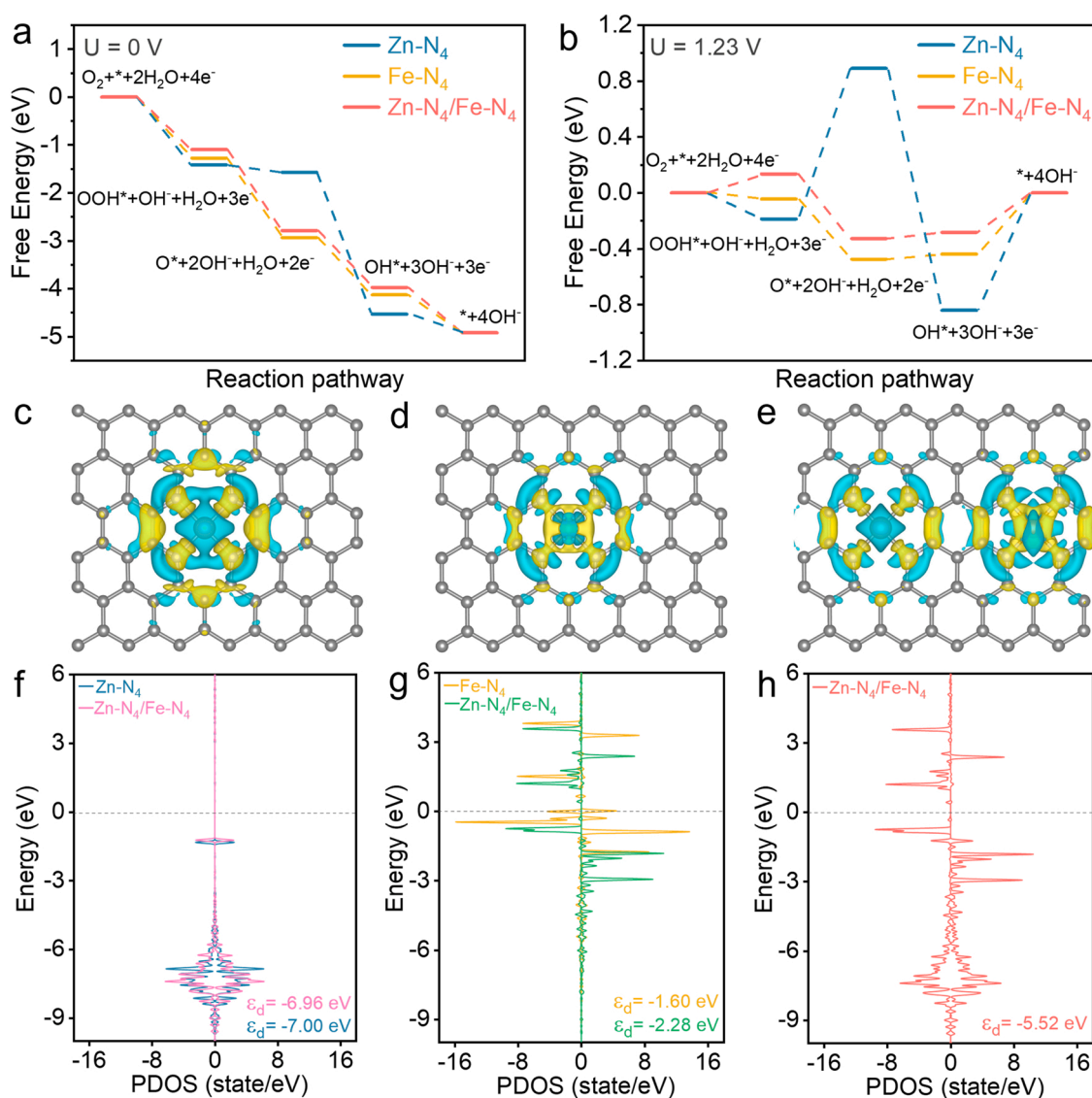

Fig. 5. Free energy diagrams of the three models at (a) U = 0 V and (b) U = 1.23 V in alkaline solution. Calculated charge density differences of (c) Zn-NC, (d) Fe-NC and (e) Zn/Fe-NC (blue: charge depletion and yellow: charge accumulation). Projected density of states for D-bands: (f) Zn in Zn-NC and in Zn/Fe-NC, (g) Fe in Fe-NC and in Zn/Fe-NC, and (h) both Fe and Zn in Zn/Fe-NC, respectively.

structures of the Fe atom and Zn atom both in the single-atom catalysts (Zn-NC and Fe-NC) and dual-atom Zn/Fe-NC catalyst were studied. The differential charge density (Fig. 5c-e) showed that more electron accumulation around the Fe atom in the dual-atom Zn/Fe-NC catalyst compared with that in Fe-NC, while a slight electron depletion around the Zn atom can be found in the dual-atom Zn/Fe-NC catalyst compared with that in Zn-NC catalyst. The electron transfer from Zn to Fe decreased the d band center of the active Fe site. As shown in Fig. 5f, the d band center of Zn in Zn-NC SAC was − 7.00 eV, thus the interaction between *O intermediate and Zn in Zn-NC SAC was very weak and the reduction of OOH* to O* was the PDS step. While the d band centers of Fe in Fe-NC SAC and dual-atom Zn/Fe-NC catalyst were − 1.60 eV and − 2.28 eV (Fig. 5g), respectively. The reduction of OH* to OH$^-$ became the PDS step, and the 0.68 eV downshifted d band center of Fe in Zn/Fe-NC decreased the adsorption of *OH more than that in Fe-NC, hence facilitating better the ORR [62,63]. Furthermore, as shown in Fig. 5f-h, the direct electronic synergistic interaction can be determined since the PDOS of both Fe and Zn atoms in the dual-atom Zn/Fe-NC are different from that in Zn-NC SAC and Fe-NC SAC.

3.4. ZABs test

To uncover the feasibility of the developed catalysts for practical applications in the energy field, ZABs were assembled using the Zn/Fe-NC catalyst supported on nickel foam as the air cathode (Fig. 6a). As depicted in Fig. 6b, the Zn/Fe-NC-based battery provided an open-circuit voltage of 1.46 V, slightly above that of the Pt/C-based ZABs (1.41 V). Besides, as depicted in the power density curves (Fig. 6c), the power density of the Zn/Fe-NC ZABs was 186.2 mW cm^{-2}, outperforming the benchmark Pt/C catalyst (149.0 mW cm^{-2}). Fig. 6d displays the rate performances of the ZABs tested by galvanostatic discharge at different current densities. Note that the Zn/Fe-NC-based ZAB exhibited higher discharge voltage at all the applied current densities, indicating a favorable rate performance. The specific capacity of the assembled ZABs was evaluated in terms of the consumed mass of Zn during a long-term galvanostatic discharge at 10 mA cm^{-2} (Fig. 6e). The specific capacity of Zn/Fe-NC-based ZAB was 814.6 mAh g^{-1},

significantly above that of Pt/C (778.6 mAh g^{-1}). Furthermore, the potential of the Zn/Fe-NC-based ZAB remains almost steady for 50 h at a discharge current density of 10 mA cm^{-2}, demonstrating excellent durability in the practical application (Fig. S22). Considering the high power and energy densities, two series-connected ZABs using Zn/Fe-NC-based cathodes were used to power 14 blue light-emitting diodes (LEDs) (Fig. 6f), demonstrating the viable application of the as-prepared catalyst.

4. Conclusion

We detailed the synthesis of bimetallic atomically dispersed Zn/Fe-NC catalysts as an efficient ORR electrocatalyst. The Zn/Fe-NC catalysts exhibited excellent activity and durability, with a high E$_{onset}$ and E$_{1/2}$ at 1.081 V and 0.875 V, respectively, and an unchanged current after 10,000 cycles in an alkaline solution. Besides, ZABs assembled with Zn/Fe-NC-based cathodes displayed a remarkable power density of 186.2 mW cm^{-2} and an outstanding specific capacity of 814.6 mAh g^{-1}. This excellent performance was related to the rich mesopore structure of the material that not only facilitates the exposure of the active sites but also the mass transfer of reactants, its high specific surface area, the high proportion of pyridine N and graphite N, and the synergistic effect obtained from the presence of the two kinds of atoms. Moreover, DFT calculations demonstrated the combination of Zn and Fe sites to favor the OH* desorption process, thus enhancing ORR activity. This work provides an effective strategy for the rational design and engineering of ZIF-derived non-precious metal catalysts with atomically dispersed dual-atom sites.

CRediT authorship contribution statement

Chuan Fu: Experimental design and data collection, Writing – original draft. **Xueqiang Qi:** Intellectual contributions to the conception, Writing – review & editing. **Tingting Yang:** Formal analysis, Visualization. **Lei Zhao:** Validation, Collection of data. **Qian Xue:** Formal analysis, Visualization. **Zhaozhao Zhu:** Data interpretation, Visualization. **Pei Xiong:** Formal analysis. **Jinxia Jiang:** Formal
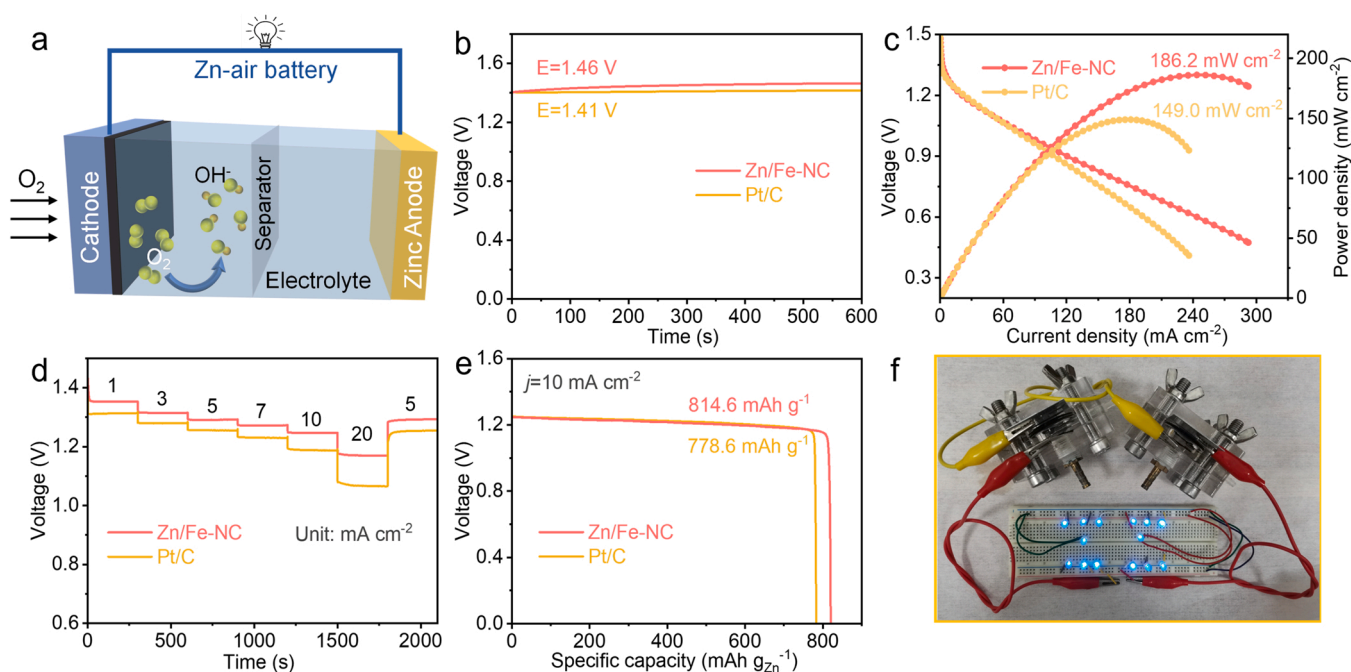
Fig. 6. (a) Schematic illustration of a ZAB. (b) Open-circuit voltage diagram of Zn/Fe-NC and Pt/C-based ZABs. (c) Discharge polarization curves and corresponding power density curves. (d) Galvanostatic discharge tests at various current densities. (e) Specific capacity measurements of Zn/Fe-NC and Pt/C-based ZABs at 10 mA cm^{-2}. (f) Photograph of blue LEDs powered by two series of ZABs using Zn/Fe-NC catalysts as the cathode.

analysis. **Xuguang An:** Formal analysis. **Haiyuan Chen:** Data interpretation. **Jun Song Chen:** Intellectual contributions to the conception. **Andreu Cabot:** Intellectual contributions to the conception, Writing – review & editing. **Rui Wu:** Intellectual contributions to the conception, Writing – review & editing.

Authorship contribution statement

The manuscript was written through contributions of all authors. All authors have given approval to the final version of the manuscript.

Declaration of Competing Interest

The authors declare that they have no known competing financial interests or personal relationships that could have appeared to influence the work reported in this paper.

Data availability

Data will be made available on request.

Acknowledgements

Appendix A. Supporting information

Supplementary data associated with this article can be found in the online version at doi:10.1016/j.apcatb.2023.122875.

References

[1] X.X. Wang, X. Yang, H. Liu, T. Han, J. Hu, H. Li, G. Wu, Air electrodes for flexible and rechargeable Zn-air batteries, Small Struct. 3 (2021) 2100103, https://doi.org/10.1002/sstr.202100103.

[2] Z. Song, J. Ding, B. Liu, X. Liu, X. Han, Y. Deng, W. Hu, C. Zhong, A rechargeable Zn-air battery with high energy efficiency and long life enabled by a highly water-retentive gel electrolyte with reaction modifier, Adv. Mater. 32 (2020) e1908127, https://doi.org/10.1002/adma.201908127.

[3] H.F. Li, L.T. Ma, C.P. Han, Z.F. Wang, Z.X. Liu, Z.J. Tang, C.Y. Zhi, Advanced rechargeable zinc-based batteries: recent progress and future perspectives, Nano Energy 62 (2019) 550–587, https://doi.org/10.1016/j.nanoen.2019.05.059.

[4] H. Yang, Y. Liu, X. Liu, X. Wang, H. Tian, G.I.N. Waterhouse, P.E. Kruger, S. G. Telfer, S. Ma, Large-scale synthesis of N-doped carbon capsules supporting atomically dispersed iron for efficient oxygen reduction reaction electrocatalysis, eScience 2 (2022) 227–234, https://doi.org/10.1016/j.esci.2022.02.005.

[5] K. Kodama, T. Nagai, A. Kuwaki, R. Jinnouchi, Y. Morimoto, Challenges in applying highly active Pt-based nanostructured catalysts for oxygen reduction reactions to fuel cell vehicles, Nat. Nanotechnol. 16 (2021) 140–147, https://doi.org/10.1038/s41565-020-00824-w.

[6] E. Proietti, F. Jaouen, M. Lefevre, N. Larouche, J. Tian, J. Herranz, J.P. Dodelet, Iron-based cathode catalyst with enhanced power density in polymer electrolyte membrane fuel cells, Nat. Commun. 2 (2011) 416, https://doi.org/10.1038/ncomms1427.

[7] X. Xu, H. Sun, S.P. Jiang, Z. Shao, Modulating metal-organic frameworks for catalyzing acidic oxygen evolution for proton exchange membrane water electrolysis, SusMat 1 (2021) 460–481, https://doi.org/10.1002/sus2.34.

[8] G. Yang, J. Zhu, P. Yuan, Y. Hu, G. Qu, B.A. Lu, X. Xue, H. Yin, W. Cheng, J. Cheng, W. Xu, J. Li, J. Hu, S. Mu, J.-N. Zhang, Regulating Fe-spin state by atomically dispersed Mn-N in Fe-N-C catalysts with high oxygen reduction activity, Nat. Commun. 12 (2021) 1734, https://doi.org/10.1038/s41467-021-21919-5.

[9] H. Jin, J. Zhu, R. Yu, W. Li, P. Ji, L. Liang, B. Liu, C. Hu, D. He, S. Mu, Tuning the Fe-N₄ sites by introducing Bi-O bonds in a Fe-N-C system for promoting the oxygen reduction reaction, J. Mater. Chem. A 10 (2022) 664–671, https://doi.org/10.1039/d1ta08256f.

[10] W. Jiang, Y. Li, Y. Xu, T. Jiang, M. Zhao, M. Deng, R. Wu, Y. Wang, Carbon nanotube-bridged N-doped mesoporous carbon nanosphere with atomic and nanoscaled M (M=Fe, Co) species for synergistically enhanced oxygen reduction reaction, Chem. Eng. J. 421 (2021) 129689, https://doi.org/10.1016/j.cej.2021.129689.

[11] M. Tong, F. Sun, Y. Xie, Y. Wang, Y. Yang, C. Tian, L. Wang, H. Fu, Operando cooperated catalytic mechanism of atomically dispersed Cu-N₄ and Zn-N₄ for promoting oxygen reduction reaction, Angew. Chem. Int. Ed. 60 (2021) 14005–14012, https://doi.org/10.1002/anie.202102053.

[12] X. Zhang, S. Zhang, Y. Yang, L. Wang, Z. Mu, H. Zhu, X. Zhu, H. Xing, H. Xia, B. Huang, J. Li, S. Guo, E. Wang, A general method for transition metal single atoms anchored on honeycomb-like nitrogen-doped carbon nanosheets, Adv. Mater. 32 (2020) 1906905, https://doi.org/10.1002/adma.201906905.

[13] X. Xie, L. Peng, H. Yang, G.I.N. Waterhouse, L. Shang, T. Zhang, MIL-101-derived mesoporous carbon supporting highly exposed fe single-atom sites as efficient oxygen reduction reaction catalysts, Adv. Mater. 33 (2021), 2101038, https://doi.org/10.1002/adma.202101038.

[14] X. Yang, C. Priest, Y. Hou, G. Wu, Atomically dispersed dual-metal-site PGM-free electrocatalysts for oxygen reduction reaction: opportunities and challenges, SusMat 2 (2022) 569–590, https://doi.org/10.1002/sus2.69.

[15] P. Rao, D. Wu, T.-J. Wang, J. Li, P. Deng, Q. Chen, Y. Shen, Y. Chen, X. Tian, Single atomic cobalt electrocatalyst for efficient oxygen reduction reaction, eScience 2 (2022) 399–404, https://doi.org/10.1016/j.esci.2022.05.004.

[16] Q. Ma, H. Jin, J. Zhu, Z. Li, H. Xu, B. Liu, Z. Zhang, J. Ma, S. Mu, Stabilizing Fe-N-C catalysts as model for oxygen reduction reaction, Adv. Sci. 8 (2021), e2102209, https://doi.org/10.1002/advs.202102209.

[17] T. Tang, S. Li, J. Sun, Z. Wang, J. Guan, Advances and challenges in two-dimensional materials for oxygen evolution, Nano Res. 15 (2022) 8714–8750, https://doi.org/10.1007/s12274-022-4575-0.

[18] X. Bai, L. Wang, B. Nan, T. Tang, X. Niu, J. Guan, Atomic manganese coordinated to nitrogen and sulfur for oxygen evolution, Nano Res. 15 (2022) 6019–6025, https://doi.org/10.1007/s12274-022-4293-7.

[19] M. Liu, H. Chun, T.-C. Yang, S.J. Hong, C.-M. Yang, B. Han, L.Y.S. Lee, Tuning the site-to-site interaction in Ru-M (M=Co, Fe, Ni) diatomic electrocatalysts to climb up the volcano plot of oxygen electroreduction, ACS Nano 16 (2022) 10657–10666, https://doi.org/10.1021/acsnano.2c02324.

[20] Y. Wang, W. Cheng, P. Yuan, G. Yang, S. Mu, J. Liang, H. Xia, K. Guo, M. Liu, S. Zhao, G. Qu, B.-A. Lu, Y. Hu, J. Hu, J.-N. Zhang, Boosting Nitrogen Reduction to ammonia on FeN₄ sites by atomic spin regulation, Adv. Sci. 8 (2021), e2102915, https://doi.org/10.1002/advs.202102915.

[21] X.B. Zhang, X. Han, Z. Jiang, J. Xu, L.N. Chen, Y.K. Xue, A.M. Nie, Z.X. Xie, Q. Kuang, L.S. Zheng, Atomically dispersed hierarchically ordered porous Fe-N-C electrocatalyst for high performance electrocatalytic oxygen reduction in Zn-Air battery, Nano Energy 71 (2020), 104547, https://doi.org/10.1016/j.nanoen.2020.104547.

[22] J. Pampel, T.P. Fellinger, Opening of bottleneck pores for the improvement of nitrogen doped carbon electrocatalysts, Adv. Energy Mater. 6 (2016), 1502389, https://doi.org/10.1002/aenm.201502389.

[23] S.H. Lee, J. Kim, D.Y. Chung, J.M. Yoo, H.S. Lee, M.J. Kim, B.S. Mun, S.G. Kwon, Y.-E. Sung, T. Hyeon, Design principle of Fe-N-C electrocatalysts: how to optimize multimodal porous structures? J. Am. Chem. Soc. 141 (2019) 2035–2045, https://doi.org/10.1021/jacs.8b11129.

[24] P. Li, X. Qi, L. Zhao, J. Wang, M. Wang, M. Shao, J.S. Chen, J. Wu, Z. Wei, Hierarchical 3D porous carbon with facilely accessible Fe-N₄ single-atom sites for Zn-air batteries, J. Mater. Chem. A 10 (2022) 5925–5929, https://doi.org/10.1039/d1ta08050d.

[25] J.X. Han, H.L. Bao, J.Q. Wang, L.R. Zheng, S.R. Sun, Z.L. Wang, C.W. Sun, 3D N-doped ordered mesoporous carbon supported single-atom Fe-N-C catalysts with superior performance for oxygen reduction reaction and zinc-air battery, Appl. Catal. B Environ. 280 (2021), 119411, https://doi.org/10.1016/j.apcatb.2020.119411.

[26] D. Xie, D. Yu, Y. Hao, S. Han, G. Li, X. Wu, F. Hu, L. Li, H.Y. Chen, Y.F. Liao, S. Peng, Dual-active sites engineering of N-doped hollow carbon nanocubes confining bimetal alloys as bifunctional oxygen electrocatalysts for flexible metal-air batteries, Small 17 (2021), e2007239, https://doi.org/10.1002/smll.202007239.

[27] J. Wang, Z. Huang, W. Liu, C. Chang, H. Tang, Z. Li, W. Chen, C. Jia, T. Yao, S. Wei, Y. Wu, Y. Li, Design of N-coordinated dual-metal sites: a stable and active Pt-free catalyst for acidic oxygen reduction reaction, J. Am. Chem. Soc. 139 (2017) 17281–17284, https://doi.org/10.1021/jacs.7b10385.

[28] M. Yang, Q. Ning, C. Fan, X. Wu, Large-scale Ni-MOF derived Ni₃S₂ nanocrystals embedded in N-doped porous carbon nanoparticles for high-rate Na⁺ storage, Chin. Chem. Lett. 32 (2020) 895–899, https://doi.org/10.1016/j.cclet.2020.07.014.

[29] C. Wang, B. Yan, J. Zheng, L. Feng, Z. Chen, Q. Zhang, T. Liao, J. Chen, S. Jiang, C. Du, S. He, Recent progress in template-assisted synthesis of porous carbons for supercapacitors, Adv. Powder Mater. 1 (2022) 100018, https://doi.org/10.1016/j.apmate.2021.11.005.

[30] Y. Ming, F. Yajing, Z. Canping, F. Junxiao, W. Shiquan, L. Jianwen, Dual-metal zeolite imidazolate framework for efficient lithium storage boosted by synergistic effects and self-assembly 2D nanosheets, Chin. Chem. Lett. 33 (2021) 3291–3295, https://doi.org/10.1016/j.cclet.2021.12.015.

[31] J. Li, M. Chen, D.A. Cullen, S. Hwang, M. Wang, B. Li, K. Liu, S. Karakalos, M. Lucero, H. Zhang, C. Lei, H. Xu, G.E. Sterbinsky, Z. Feng, D. Su, K.L. More, G. Wang, Z. Wang, G. Wu, Atomically dispersed manganese catalysts for oxygen reduction in proton-exchange membrane fuel cells, Nat. Catal. 1 (2018) 935–945, https://doi.org/10.1038/s41929-018-0164-8.

[32] J. Zhu, S. Mu, Active site engineering of atomically dispersed transition metal-heteroatom-carbon catalysts for oxygen reduction, Chem. Commun. 57 (2021) 7869–7881, https://doi.org/10.1039/d1cc03076k.

[33] Y.Y. Li, P.Y. Zhang, L.Y. Wan, Y.P. Zheng, X.M. Qu, H.K. Zhang, Y.S. Wang, K. Zaghib, J.Y. Yuan, S.H. Sun, Y.C. Wang, Z.Y. Zhou, S.G. Sun, A general

carboxylate-assisted approach to boost the ORR performance of ZIF-derived Fe/N/C catalysts for proton exchange membrane fuel cells, Adv. Funct. Mater. 31 (2021), 2009645, https://doi.org/10.1002/adfm.202009645.

[34] S. Ibraheem, S. Chen, L. Peng, J. Li, L. Li, Q. Liao, M. Shao, Z. Wei, Strongly coupled iron selenides-nitrogen-bond as an electronic transport bridge for enhanced synergistic oxygen electrocatalysis in rechargeable zinc-O_2 batteries, Appl. Catal. B Environ. 265 (2020), 118569, https://doi.org/10.1016/j.apcatb.2019.118569.

[35] Y. Liang, Y. Li, H. Wang, J. Zhou, J. Wang, T. Regier, H. Dai, Co_3O_4 nanocrystals on graphene as a synergistic catalyst for oxygen reduction reaction, Nat. Mater. 10 (2011) 780–786, https://doi.org/10.1038/Nmat3087.

[36] J.X. Zhao, Z.F. Chen, Single Mo atom supported on defective boron nitride monolayer as an efficient electrocatalyst for nitrogen fixation: a computational study, J. Am. Chem. Soc. 139 (2017) 12480–12487, https://doi.org/10.1021/jacs.7b05213.

[37] H. Yin, P. Yuan, B.-A. Lu, H. Xia, K. Guo, G. Yang, G. Qu, D. Xue, Y. Hu, J. Cheng, S. Mu, J.-N. Zhang, Phosphorus-driven electron delocalization on edge-type FeN_4 Active sites for oxygen reduction in acid medium, ACS Catal. 11 (2021) 12754–12762, https://doi.org/10.1021/acscatal.1c02259.

[38] X. Chen, D.-D. Ma, B. Chen, K. Zhang, R. Zou, X.-T. Wu, Q.-L. Zhu, Metal-organic framework-derived mesoporous carbon nanoframes Embedded with atomically dispersed Fe-Nx active sites for efficient bifunctional oxygen and carbon dioxide electroreduction, Appl. Catal. B Environ. 267 (2020), 118720, https://doi.org/10.1016/j.apcatb.2020.118720.

[39] Q.X. Lai, Y.X. Zhao, Y.Y. Liang, J.P. He, J.H. Chen, In situ confinement pyrolysis transformation of ZIF-8 to nitrogen-enriched meso-microporous carbon frameworks for oxygen reduction, Adv. Funct. Mater. 26 (2016) 8334–8344, https://doi.org/10.1002/adfm.201603607.

[40] Y. He, S. Hwang, D.A. Cullen, M.A. Uddin, L. Langhorst, B. Li, S. Karakalos, A. J. Kropf, E.C. Wegener, J. Sokolowski, M. Chen, D. Myers, D. Su, K.L. More, G. Wang, S. Litster, G. Wu, Highly active atomically dispersed CoN_4 fuel cell cathode catalysts derived from surfactant-assisted MOFs: carbon-shell confinement strategy, Energy Environ. Sci. 12 (2019) 250–260, https://doi.org/10.1039/c8ee02694g.

[41] Y. He, X. Yang, Y. Li, L. Liu, S. Guo, C. Shu, F. Liu, Y. Liu, Q. Tan, G. Wu, Atomically dispersed Fe-Co dual metal sites as bifunctional oxygen electrocatalysts for rechargeable and flexible Zn-air batteries, ACS Catal. 12 (2022) 1216–1227, https://doi.org/10.1021/acscatal.1c04550.

[42] C. Liu, T. Li, X. Dai, J. Zhao, D. He, G. Li, B. Wang, X. Cui, Catalytic activity enhancement on alcohol dehydrogenation via directing reaction pathways from single-to double-atom catalysis, J. Am. Chem. Soc. 144 (2022) 4913–4924, https://doi.org/10.1021/jacs.1c12705.

[43] H. Zhang, H.T. Chung, D.A. Cullen, S. Wagner, U.I. Kramm, K.L. More, P. Zelenay, G. Wu, High-performance fuel cell cathodes exclusively containing atomically dispersed iron active sites, Energy Environ. Sci. 12 (2019) 2548–2558, https://doi.org/10.1039/c9ee00877b.

[44] U.I. Kramm, I. Herrmann-Geppert, S. Fiechter, G. Zehl, I. Zizak, I. Dorbandt, D. Schmeißer, P. Bogdanoff, Effect of iron-carbide formation on the number of active sites in Fe-N-C catalysts for the oxygen reduction reaction in acidic media, J. Mater. Chem. A 2 (2014) 2663–2670, https://doi.org/10.1039/C3TA13821F.

[45] L. Zhao, J. Jiang, S. Xiao, Z. Li, J. Wang, X. Wei, Q. Kong, J.S. Chen, R. Wu, PtZn nanoparticles supported on porous nitrogen-doped carbon nanofibers as highly stable electrocatalysts for oxygen reduction reaction, Nano Mater. Sci. (2022), https://doi.org/10.1016/j.nanoms.2022.04.001.

[46] F.T. Kong, Y.F. Huang, M.X. Chen, G. Meng, H. Tian, Y.F. Chen, Z.W. Chang, C. Chen, W.P. Sun, X.Z. Cui, J.L. Shi, Creation of densely exposed and cavity-edged single Fe active sites for enhanced oxygen electroreduction, Appl. Catal. B Environ. 317 (2022), 121768, https://doi.org/10.1016/j.apcatb.2022.121768.

[47] Z. Zhu, Z. Li, J. Wang, R. Li, H. Chen, Y. Li, J.S. Chen, R. Wu, Z. Wei, Improving NiN_X and pyridinic N active sites with space-confined pyrolysis for effective CO_2 electroreduction, eScience 2 (2022) 445–452, https://doi.org/10.1016/j.esci.2022.05.002.

[48] H. Zhang, S. Hwang, M. Wang, Z. Feng, S. Karakalos, L. Luo, Z. Qiao, X. Xie, C. Wang, D. Su, Y. Shao, G. Wu, Single atomic iron catalysts for oxygen reduction

[49] in acidic media: particle size control and thermal activation, J. Am. Chem. Soc. 139 (2017) 14143–14149, https://doi.org/10.1021/jacs.7b06514.

[49] J. Xue, Y. Li, J. Hu, Nanoporous bimetallic Zn/Fe-N-C for efficient oxygen reduction in acidic and alkaline media, J. Mater. Chem. A 8 (2020) 7145–7157, https://doi.org/10.1039/c9ta13471a.

[50] Y. Zhou, G. Chen, Q. Wang, D. Wang, X. Tao, T. Zhang, X. Feng, K. Müllen, Fe-N-C electrocatalysts with densely accessible $Fe-N_4$ sites for efficient oxygen reduction reaction, Adv. Funct. Mater. 31 (2021), 2102420, https://doi.org/10.1002/adfm.202102420.

[51] X. Wu, Q. Wang, S. Yang, J. Zhang, Y. Cheng, H. Tang, L. Ma, X. Min, C. Tang, S. P. Jiang, F. Wu, Y. Lei, S. Ciampic, S. Wang, L. Dai, Sublayer-enhanced atomic sites of single atom catalysts through in situ atomization of metal oxide nanoparticles, Energy Environ. Sci. 15 (2022) 1183–1191, https://doi.org/10.1039/d1ee03311e.

[52] Z.D. Wang, S. Liang, C.K. Bai, Z.F. Guo, G.L. Lu, H. Sun, Z.N. Liu, H.Y. Zang, Synergistically enhanced iron and zinc bimetallic sites as an advanced ORR electrocatalyst for flow liquid rechargeable Zn-air batteries, J. Mater. Chem. A 10 (2022) 3169–3177, https://doi.org/10.1039/d1ta09678h.

[53] L. Xu, D. Deng, Y. Tian, H. Li, J. Qian, J. Wu, H. Li, Dual-active-sites design of CoN_x anchored on zinc-coordinated nitrogen-codoped porous carbon with efficient oxygen catalysis for high-stable rechargeable zinc-air batteries, Chem. Eng. J. 408 (2020), 127321, https://doi.org/10.1016/j.cej.2020.127321.

[54] S. Yin, S. Yang, G. Li, G. Li, B. Zhang, C. Wang, M. Chen, H.-G. Liao, J. Yang, Y. Zhang, S.-G. Sun, Seizing gaseous Fe^{2+} to densify O_2-accessible $Fe-N_4$ sites for high-performance proton exchange membrane fuel cells, Energy Environ. Sci. 15 (2022) 3033–3040, https://doi.org/10.1039/d2ee00061j.

[55] D. Xue, J. Cheng, P. Yuan, B.A. Lu, H. Xia, C.C. Yang, C.L. Dong, H. Zhang, F. Shi, S. Mu, J. Hu, S. Sun, J.-N. Zhang, Boron-tethering and regulative Electronic states around iridium species for hydrogen evolution, Adv. Funct. Mater. 32 (2022), 2113191, https://doi.org/10.1002/adfm.202113191.

[56] L. Han, S. Song, M. Liu, S. Yao, Z. Liang, H. Cheng, Z. Ren, W. Liu, R. Lin, G. Qi, X. Liu, Q. Wu, J. Luo, H.L. Xin, Stable and efficient single-atom Zn catalyst for CO_2 reduction to CH_4, J. Am. Chem. Soc. 142 (2020) 12563–12567, https://doi.org/10.1021/jacs.9b12111.

[57] Z. Zhang, J. Sun, F. Wang, L. Dai, Efficient oxygen reduction reaction (ORR) catalysts based on single iron atoms dispersed on a hierarchically structured porous carbon framework, Angew. Chem. Int. Ed. 57 (2018) 9038–9043, https://doi.org/10.1002/anie.201804958.

[58] G. Han, Y. Zheng, X. Zhang, Z. Wang, Y. Gong, C. Du, M.N. Banis, Y.-M. Yiu, T.-K. Sham, L. Gu, Y. Sun, Y. Wang, J. Wang, Y. Gao, G. Yin, X. Sun, High loading single-atom Cu dispersed on graphene for efficient oxygen reduction reaction, Nano Energy 66 (2019), 104088, https://doi.org/10.1016/j.nanoen.2019.104088.

[59] S. Huang, Z. Qiao, P. Sun, K. Qiao, K. Pei, L. Yang, H. Xu, S. Wang, Y. Huang, Y. Yan, D. Cao, The strain induced synergistic catalysis of FeN_4 and MnN_3 dual-site catalysts for oxygen reduction in proton- /anion- exchange membrane fuel cells, Appl. Catal. B Environ. 317 (2022), 121770, https://doi.org/10.1016/j.apcatb.2022.121770.

[60] Q. Wang, L. Shang, R. Shi, X. Zhang, Y. Zhao, G.I.N. Waterhouse, L.-Z. Wu, C.-H. Tung, T. Zhang, NiFe layered double hydroxide nanoparticles on Co,N-codoped carbon nanoframes as efficient bifunctional catalysts for rechargeable zinc-air batteries, Adv. Energy Mater. 7 (2017), 1700467, https://doi.org/10.1002/aenm.201700467.

[61] C. Zheng, X. Zhang, Z. Zhou, Z. Hu, A first-principles study on the electrochemical reaction activity of 3d transition metal single-atom catalysts in nitrogen-doped graphene: trends and hints, eScience 2 (2022) 219–226, https://doi.org/10.1016/j.esci.2022.02.009.

[62] B.Y. Xia, S. Zaman, Y.-Q. Su, C.-L. Dong, R. Qi, L. Huang, Y. Qin, Y.-C. Huang, F.-m Li, B. You, W. Guo, Q. Li, S. Ding, Scalable molten salt synthesis of platinum alloys planted in metal-nitrogen-graphene for efficient oxygen reduction, Angew. Chem. Int. Ed. 61 (2021), e202115835, https://doi.org/10.1002/anie.202115835.

[63] J. Xu, S. Lai, D. Qi, M. Hu, X. Peng, Y. Liu, W. Liu, G. Hu, H. Xu, F. Li, Atomic Fe-Zn dual-metal sites for high-efficiency pH-universal oxygen reduction catalysis, Nano Res. 14 (2021) 1374–1381, https://doi.org/10.1007/s12274-020-3186-x.